

PAPER • OPEN ACCESS

Graphene-induced invertible magnetoresistance in variable phase iron oxides

To cite this article: N Schulz *et al* 2026 *J. Phys.: Condens. Matter* **38** 145803

View the [article online](#) for updates and enhancements.

You may also like

- [Electric-field-induced extremely large change in resistance in graphene ferromagnets](#)
Yu Song
- [Proximity induced room temperature ferromagnetism in graphene probed with spin currents](#)
Johannes Christian Leutenantsmeyer, Alexey A Kaverzin, Magdalena Wojtaszek et al.
- [Charge-transfer-induced 2D ferromagnetism and realization of thermomnant memory effect in ultrathin \$\beta\$ -NiOOH-encapsulated graphene](#)
Shatabda Bhattacharya, Woojin Choi, Antara Ghosh et al.



PAPER

OPEN ACCESS

RECEIVED
24 April 2025REVISED
6 January 2026ACCEPTED FOR PUBLICATION
30 March 2026PUBLISHED
13 April 2026

Original content from this work may be used under the terms of the [Creative Commons Attribution 4.0 licence](#).

Any further distribution of this work must maintain attribution to the author(s) and the title of the work, journal citation and DOI.



Graphene-induced invertible magnetoresistance in variable phase iron oxides

N Schulz^{1,2} , D DeTellem², A Chanda^{2,3} , G Datt⁴, A Ojo² , D A Arena² , H R Gutierrez² , T Sarkar⁴, M V Kamalakar⁵ , S Witanachchi², M H Phan^{2,6} and H Srikanth^{2,*} ¹ Naval Surface Warfare Center Panama City Division, Panama City, FL 32407, United States of America² Department of Physics, University of South Florida, Tampa, FL 33620, United States of America³ Department of Energy Conversion and Storage, Technical University of Denmark, Kongens Lyngby 2800, Denmark⁴ Department of Materials Science and Engineering, Uppsala University, Box 35, SE-751 03 Uppsala, Sweden⁵ Department of Physics and Astronomy, Uppsala University, SE-751 20 Uppsala, Sweden⁶ Center for Materials Innovation and Technology, VinUniversity, Hanoi 100000, Vietnam

* Author to whom any correspondence should be addressed.

E-mail: sharihar@usf.edu**Keywords:** iron oxide, graphene, magnetoresistive switching, percolative transportSupplementary material for this article is available [online](#)**Abstract**

Iron oxides are one of the oldest magnetic systems in history and have been studied extensively due to their phase-tunable magnetic and electronic properties. The combination of ferrimagnetic half-metallic magnetite (Fe_3O_4) with antiferromagnetic insulating hematite ($\alpha\text{-Fe}_2\text{O}_3$) forms a so-called biphasic iron oxide (BPIO) system that exhibits highly tunable magnetic and spin-transport properties in terms of phase and volume fraction. In this work, we report the interfacial physics between variations of these iron oxide phases with graphene (Gr) on magnetotransport in these heterostructures. Our experiments reveal that the inclusion of graphene in these heterostructures induces an inversion in the sign of magnetoresistance at finite temperatures. We explain this observation with an effective percolative transport model. Interestingly, the switching temperature and the sharpness of the transition can be further tuned by varying the phase volume fractions of the iron oxide layer and the crystallinity. The BPIO films, which grow naturally on Si substrates, exhibit the highest switching temperature. Our observations underscore the ability to induce magnetoresistive switching in abundant iron oxide grown on cost-effective, CMOS-compatible substrates by including a single layer of Gr, which has potential applications in modern devices and neuromorphic computing.

1. Introduction

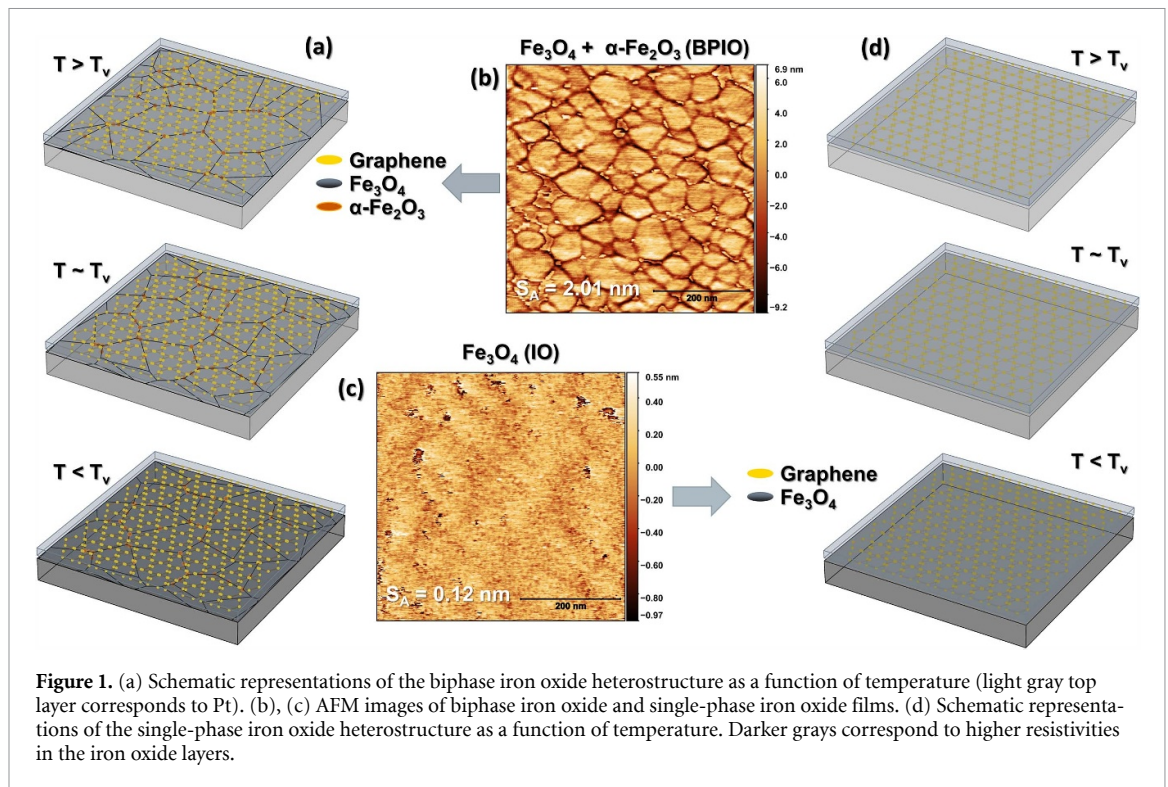
Different polymorphs of iron oxide have been shown to exhibit unique temperature and phase-dependent properties [1, 2], which have been leveraged for applications in devices [3, 4], medical treatment [5], water filtration [6, 7], etc. Of the various polymorphs of iron oxide, magnetite (Fe_3O_4), and hematite ($\alpha\text{-Fe}_2\text{O}_3$) are two of the most commonly studied due to their natural abundance and temperature dependent magnetic and electronic properties. Magnetite exhibits a characteristic metal-insulator transition known as the Verwey transition ($T_V \approx 120$ K), for which it is insulating below T_V and conducting/semiconducting above T_V [8, 9]. On the other hand, single crystalline hematite is an antiferromagnetic insulator, which exhibits a first order spin reorientation transition known as the Morin transition ($T_M \approx 260$ K) [10]. This transition, however, has been shown to be thickness dependent, decreasing in temperature with film thickness [8, 11–13].

The control of these various phases in both thin film and nanoparticle form has been extensively studied [1, 14]. For thin films of iron oxide, it has been shown that through the control of growth parameters and importantly, choice of substrate, different phases of iron oxide can be grown with different degrees of crystallinity. For example, Fe_3O_4 and $\alpha\text{-Fe}_2\text{O}_3$ may be grown epitaxially through the choice

of MgO (100) and $\alpha - \text{Al}_2\text{O}_3$ (0001) substrates, respectively, supporting proper lattice matching [15, 16]. Furthermore, a mixture of both (IO) and, so called biphasic iron oxide (BPIO) [17], can be grown by the choice of Si (100) substrates which gives rise to the biphasic behavior through lattice mismatch-induced strain [8, 18]. The intentional choice of substrate which produces BPIO has been shown to give rise to the ability to observe competing magnetic interactions, surface-mediated spin transport phenomena, and exotic temperature dependent magnetic properties [8, 18]. Furthermore, Si substrates are far more cost effective and are compatible with existing CMOS technologies for device applications.

The magnetic and electronic properties of variable phase iron oxides have been extended to further applications through functionalizing to different morphologies and heterostructures [3–7, 19]. A possible opportunity for further functionalization for applications is the inclusion of two-dimensional (2D) materials, of which graphene (Gr), a 2D allotrope of carbon, has been of particular interest [4, 6, 19]. This is largely due to the exotic electronic and magnetic properties exhibited by Gr [20, 21], including the hosting of Dirac fermions [22], low intrinsic spin–orbit coupling [23], unique interfacial magnetic behavior [24, 25] etc. These aspects render graphene an ideal medium of spin transport over tens of microns at room temperature [26]. Magnetoresistance (MR) in pure graphene has been studied extensively [27–29] as a function of temperature [30], for CVD graphene [28], as well as in non-local measurements [31]. Recent advancements and challenges in graphene-based spintronics research have been comprehensively discussed in a recent review article [32] with inversion effects in MR in graphene spin valves [33]. The interfacial effects of graphene with conventional oxides also display intricate charge transfer mechanisms and enhanced performance in devices [34]. However, the nature of the interfacial magnetism in iron oxide/Gr heterostructures is not well understood, particularly for the various phases of iron oxide. Understanding the nature of magnetism and magnetotransport across the phase-tunable iron oxide/Gr interface can be used to harbor new physics not yet uncovered for novel device applications.

Here, the change in the temperature-dependent magnetic and electronic properties of 100 nm thick phase-tunable iron oxide (Fe_3O_4 and BPIO) due to the inclusion of monolayer Gr, capped with a protective 5 nm thick Pt is explored. This was done by utilizing both surface and bulk sensitive measurements. Temperature-dependent magnetization measurements indicate the existence of the aforementioned characteristic Verwey and Morin transitions at T_V , almost equal to 120 K, and $T_M \approx 260\text{K}$, occurring in their respective samples. The inclusion of Gr induces strong interfacial coupling in the BPIO sample, as observed via the dampening of the Verwey transition as compared to the BPIO/Pt system. To further explore the nature of these changes, surface-sensitive longitudinal MR and resistivity measurements were performed as a function of temperature in a standard four-point configuration. While the BPIO/Pt and IO/Pt samples have similar MR as previously reported to their non-Gr counterparts [8, 35–37], IO/Gr/Pt and BPIO/Gr/Pt exhibit a switching of the sign of the MR at different temperatures. To further explore this behavior, resistivity versus temperature measurements were performed. While the BPIO/Pt and IO/Pt systems exhibited similar behavior as previously observed, BPIO/Gr/Pt and IO/Gr/Pt exhibit a peak in the temperature-dependent resistivity, similar to that of colossal MR (CMR) observed in doped manganites, occurring at the temperatures in which their MRs change sign [38, 39]. For each system, the temperature dependent resistivity is fit to determine the relevant scattering mechanisms. In BPIO/Gr/Pt and IO/Gr/Pt, a modified percolation model is used to describe the critical behavior of the resistivity [40]. The resistivity results indicate that the inclusion of Gr induces interfacial coupling through surface hybridization with the underlying BPIO/IO layer, when the system is in an insulating state. The different temperature dependent configurations of each system can be seen schematically in figures 1(a) and (d), and physically through atomic force microscopy (AFM) on the magnetic substrate layers in figures 1(b) and (c). As seen in figures 1(b) and (c), the IO films show no appreciable grain boundaries as expected for highly crystalline systems; however, for BPIO, there are clear grain boundaries, and it seems that in between the grain boundaries, seeds of hematite form. This gives rise to metallic-paramagnetic (PM) transport in the Pt layer and insulating-magnetic transport at the Gr/BPIO(IO) interface. This interface leads to effective percolative transport due to competition between localized and delocalized carriers. When the energy difference between the two phases is close, the peak in the resistivity and switching of the MR occurs. The difference in the switching temperatures between the IO and BPIO systems is then understood as different volume fractions of insulating phases, where in the IO sample, the switching does not occur until close to T_V . These results elucidate the nature of the interfacial magnetism in varying phase iron oxide/Gr systems. These results provide proof of principle that by including Gr as a means for modifying phase segregated systems, interfacially induced colossal-like MR can occur. Such behavior can be used to design new devices for applications in magnetoresistive switching and neuromorphic computing.



2. Results and discussion

To confirm the phase determination in the films both x-ray diffraction (XRD) and Raman spectroscopy measurements were performed at room temperature. It is important to note that since hematite can occur as a small minority phase, multiple measurements confirming the phase purity must be performed. Figures 2(a)–(c) shows the Raman spectra for BPIO/Pt, BPIO/Gr/Pt, and IO/Gr/Pt, respectively prior to sputtering Pt, with the insets zooming in around the respective peaks for scale. Peaks for magnetite and hematite are identified from previously reported values, in which hematite exhibits a strong peak at $\sim 612 \text{ cm}^{-1}$. Magnetite exhibits a strong peak at $\sim 668 \text{ cm}^{-1}$. In the case of the films grown on Si/SiO₂, the scale of the peaks is reduced with respect to the strong Si peak around 500 cm^{-1} (all graphs are on a linear y -scale). In the pure IO film, a secondary weaker peak at $\sim 550 \text{ cm}^{-1}$ is observed since it is not overlapping with the Si peak [41]. Furthermore, it can be seen in figures 2(b) and (c) that the strong primary peak of Gr at $\sim 1580 \text{ cm}^{-1}$ due to the in-plane motion of the carbon atoms is observed as expected. Figure S1 shows the Raman spectra of the BPIO/Gr/Pt system after sputtering, where a D peak appears likely due to sputtering induced out-of-plane motion of the carbon atoms [42]. Importantly, the Gr peaks are observed in the films with Gr, as expected, and the BPIO films show both magnetite and hematite peaks, while the single-phase IO film shows just magnetite peaks.

Figures 2(d)–(f) shows the XRD spectra for BPIO/Pt, BPIO/Gr/Pt, and IO/Gr/Pt, respectively. In the BPIO films, multiple reflections can be seen showing clear indication of the polycrystalline nature of the films. Furthermore, both magnetite and hematite phases are identified through their respective crystal structures. In the single-phase IO film, only the [220] orientation of IO arises as expected [17]. Combining both the XRD and Raman spectra results confirms the hypothesis that the biphasic films contain both magnetite and hematite, and the single-phase film is just magnetite.

The bulk magnetic properties of each of the films were then characterized. Figures 3(a)–(c) shows the magnetic susceptibility versus temperature ($\chi(T)$) following the zero-field-cooled (ZFC) and field-cooled (FC) measurement protocols for IO/Gr/Pt, BPIO/Pt, and BPIO/Gr/Pt, respectively. BPIO/Pt and BPIO/Gr/Pt exhibit both the Verwey and Morin transitions as expected, identified as inflections in the susceptibility versus temperature for the Morin transition, and a decrease in the susceptibility below the Verwey transition as has been previously reported [8]. As compared to the BPIO/Pt film, the BPIO/Gr/Pt film shows a weaker Verwey transition. The IO/Gr/Pt film does not appear to have a strong Verwey transition and exhibits changes in the magnetization around low temperature indicative of spin freezing which has been previously reported [43].

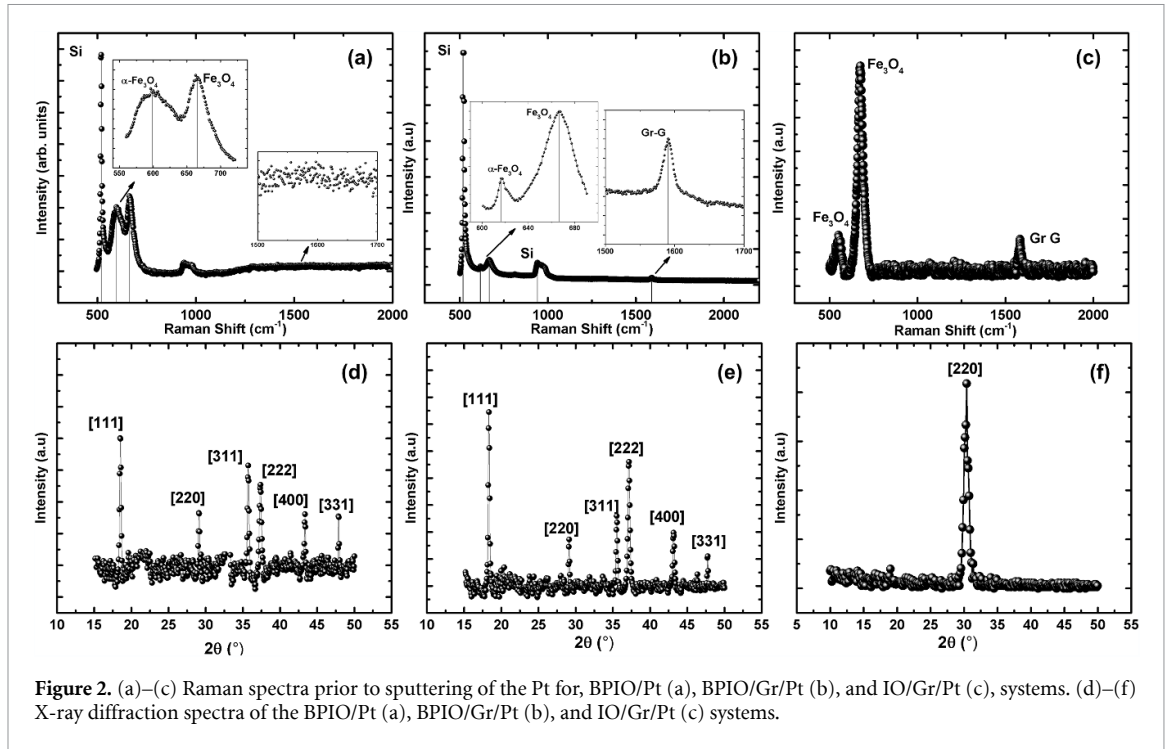


Figure 2. (a)–(c) Raman spectra prior to sputtering of the Pt for, BPIO/Pt (a), BPIO/Gr/Pt (b), and IO/Gr/Pt (c), systems. (d)–(f) X-ray diffraction spectra of the BPIO/Pt (a), BPIO/Gr/Pt (b), and IO/Gr/Pt (c) systems.

It should be noted that since the IO films are grown on MgO, there exists a strong low temperature background to the $\chi(T)$ measurement, and it is expected that the single-phase films exhibit a strong Verwey transition. To confirm this phenomenon, resistance versus temperature measurements were performed on bare IO films from the same sample batch, shown in figure S2 in the supporting information. There exists a strong increase in the resistance versus temperature in the IO film, indicative of a strong Verwey transition as expected. It should be noted that data are only presented up to $T \sim 100$ K, since the metal-insulator transition was so strong that it exceeded the measurable resistance in our system. Figures 3(d) and (e) show the magnetization versus magnetic field ($M(H)$) at $T = 300$ and 10 K, respectively. At room temperature, there is not a large difference between the bulk magnetic properties, outside small changes in the anisotropy. However, at lower temperatures there exists subtle differences, as identified by slope changes around the coercive field $H_c \sim 0.20$ T. The IO/Gr/Pt film exhibits glassy-like behavior identified as via nonlinear changes in the magnetization around low fields, similar to what is observed in the $M(T)$ curve. Previous reports have revealed glassy behavior at interfaces in thin film heterostructures of IO, as identified through exchange-bias measurements [18, 44]. Importantly, correlating with previous results it appears that this low temperature behavior is intrinsic to the bulk magnetic properties of IO. These measurements are background corrected for the substrate contributions, so this confirms the intrinsic nature of the glassy behavior to the IO/Gr/Pt film.

To probe the nature of the interfacial magnetism between graphene and the variable phase iron oxide films, longitudinal MR measurements were performed in a standard four-point connection, as a function of temperature. It should be noted that due to the large difference in respective thicknesses of the top metallic layer as compared to the iron oxide layers, there exists non-zero current shunted through the oxide layer. Figures 4(a)–(f) shows the temperature dependence of the MR for BPIO/Pt, BPIO/Gr/Pt, and IO/Gr/Pt, respectively. The BPIO/Pt films exhibit negative MR as has been reported previously [35, 45]. It can be seen in comparison to figures 3(d) and (e) that while there are no appreciable room temperature differences in the bulk magnetization as a function of field, their surface properties differ significantly. This negative MR arises due to the spin dependent scattering across magnetic domains, due to uneven local directions of the magnetization [8]. Based on the spin-direction of the carrier with respect to the direction of the magnetization of the magnetic domains nearby, higher or lower resistance will occur. As a higher magnetic field is applied, the domains become more uniformly magnetized and the resistance decreases. For the BPIO/Gr/Pt and IO/Gr/Pt films, a similar phenomenon occurs at room temperature. Namely, negative MR occurs in both films at high temperature, in agreement with the homogeneity of the magnetization versus magnetic field results. However, as temperature is decreased, values of MR for both the BPIO/Gr/Pt and IO/Gr/Pt films homogeneously approach zero, then the sign changes. It should be noted that the temperatures in which the MR switches sign are different between

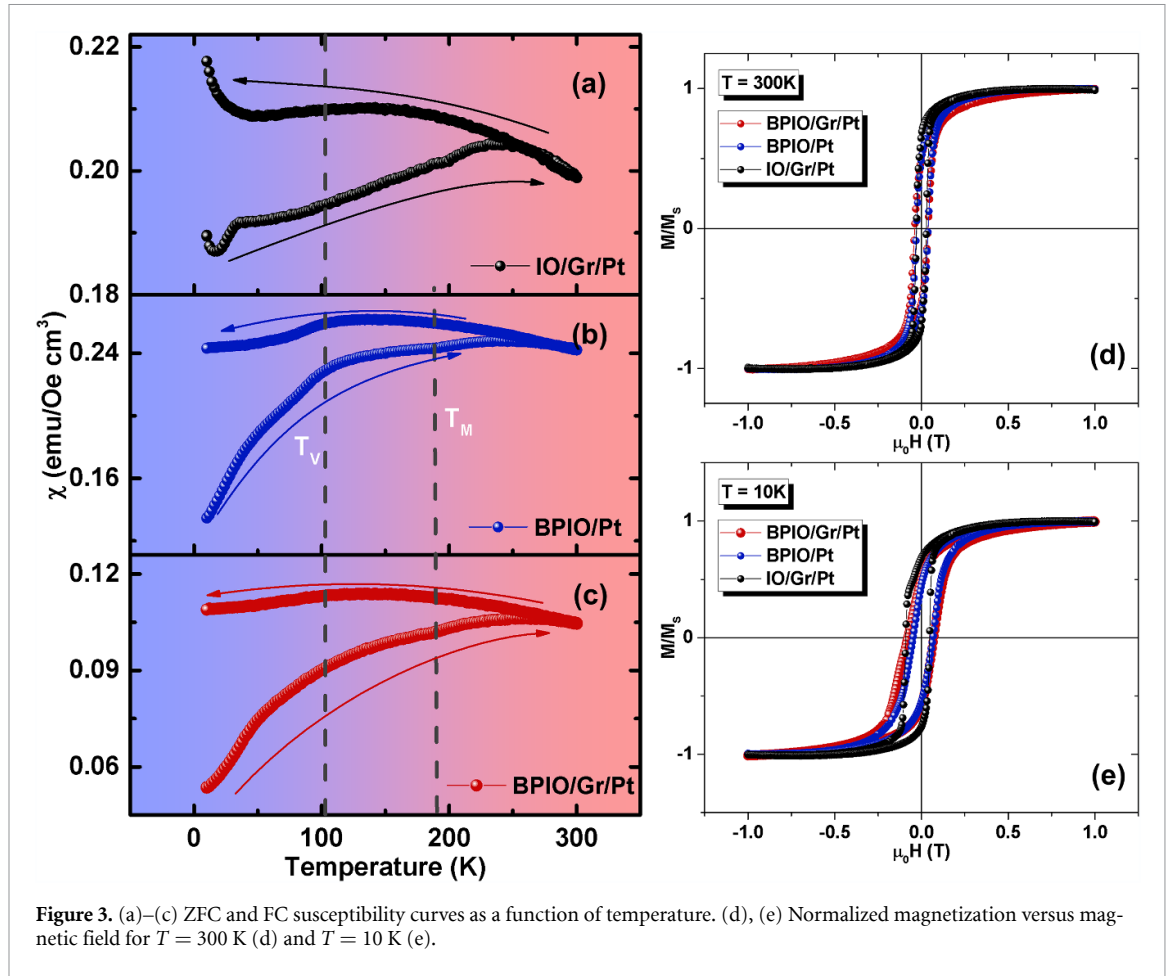


Figure 3. (a)–(c) ZFC and FC susceptibility curves as a function of temperature. (d), (e) Normalized magnetization versus magnetic field for $T = 300\text{ K}$ (d) and $T = 10\text{ K}$ (e).

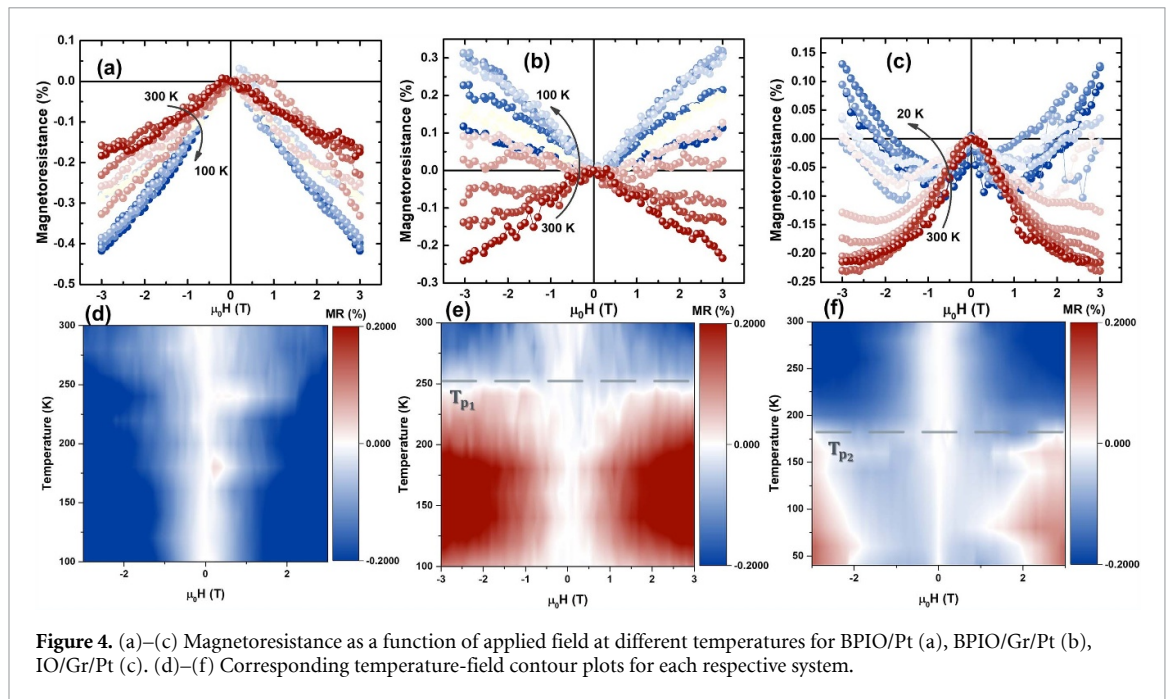
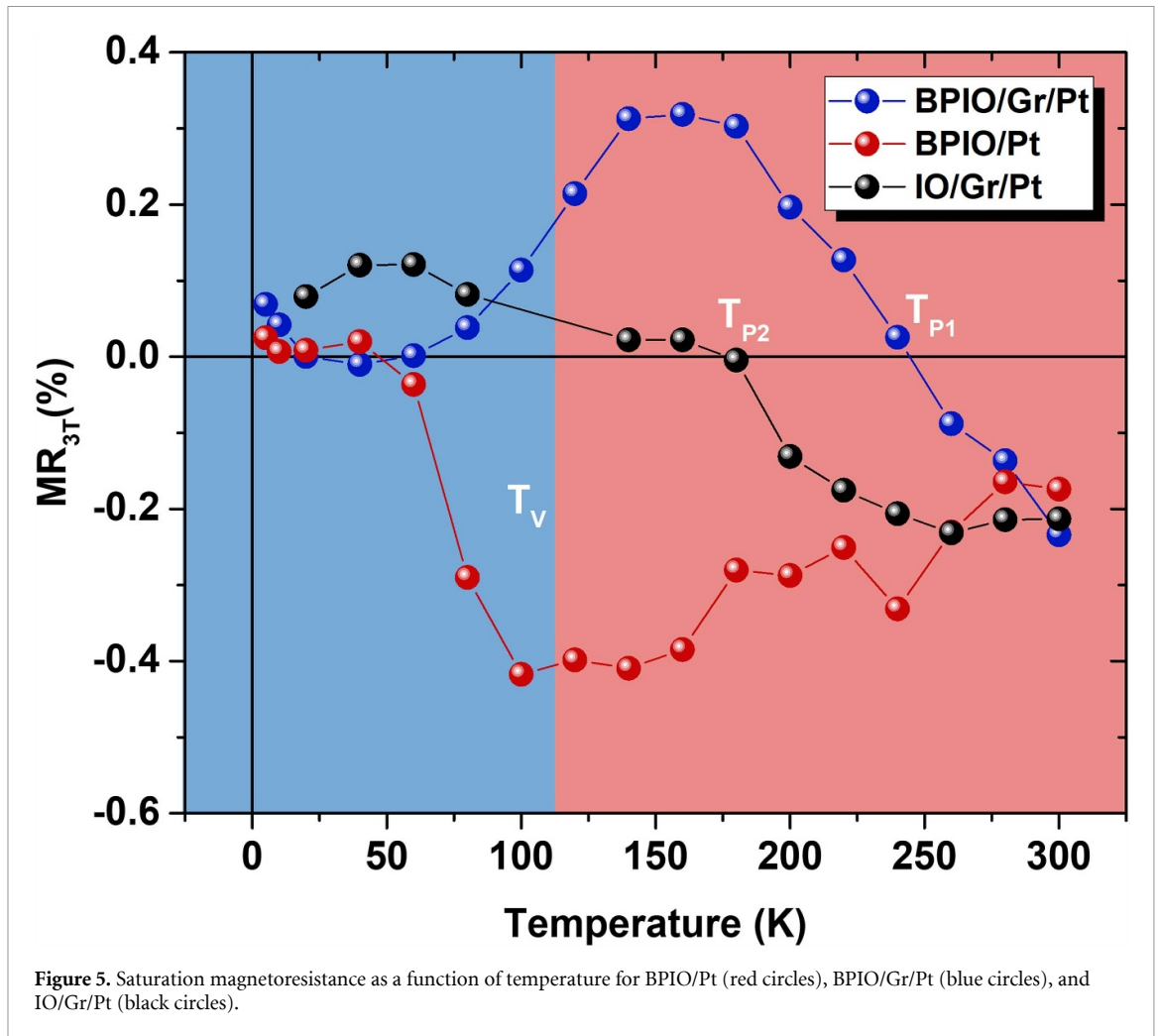


Figure 4. (a)–(c) Magnetoresistance as a function of applied field at different temperatures for BPIO/Pt (a), BPIO/Gr/Pt (b), IO/Gr/Pt (c). (d)–(f) Corresponding temperature-field contour plots for each respective system.

the films, however, with BPIO/Gr/Pt and IO/Gr/Pt switching at $T_{p1} \sim 250\text{ K}$ and $T_{p2} \sim 180\text{ K}$, respectively. This underscores the impact of the secondary hematite phase in the tuning of the surface magnetic properties in these films, and its impact on the switching temperature of the MR.

Furthermore, the MR as a function of temperature was measured for pure IO/Pt, to confirm that this behavior is not intrinsic to the IO/Pt interface. Figure S3(a) in the supporting information shows the



temperature dependence of the MR for IO/Pt and (b) shows the saturation MR as a function of temperature. It can be seen that there is no temperature dependent switching of the MR intrinsic for IO/Pt. Furthermore, in figure S3(b) in the supporting information, the value of the saturation MR becomes more negative with a decrease in temperature, with a critical point at the Verwey transition, as expected [8]. These results indicate that the inclusion of Gr is inducing the temperature dependent inversion in the MR, and that the temperature at which this occurs is sensitive to the relative phase fractions of magnetite and hematite. To further confirm this behavior, identical BPIO/Gr/Pt films with different fractions of magnetite and hematite were fabricated, which can be seen in figure S4 in the supporting information.

As seen in figure S4, in the second BPIO/Gr/Pt film, inversion in the MR occurs again. Here, the temperature in which the inversion occurs is slightly lower than that of the other film with $T_{p3} \sim 180$ K. This underscores the reproducible nature of this phenomenon. Furthermore, these results suggest that the inversion temperature can be controlled by changing the relative phases of magnetite and hematite. It is possible that this boils down to changing the oxygen percentage since changing the relative phase fractions will necessarily change the oxygen percentage (magnetite O % $\sim 57\%$, hematite O % $\sim 60\%$), which was realized here by adjusting the laser fluence, and it is expected that for both systems in insulating states, the majority of the states near the Fermi energy are oxygen states and therefore play a large role in the interfacial properties [46, 47]. In the case of the BPIO films, the existence of insulating hematite at $T > T_v$ may act as a seed layer for Gr hybridization, allowing the switching to occur at higher temperatures. These results are encapsulated in figure 5, where the saturation MR as a function of temperature is plotted for all 3 samples. In figure 5, it can be clearly seen where the MR changes sign is higher for the BPIO/Gr/Pt sample as compared to the IO/Gr/Pt sample. Furthermore, both the BPIO samples increase in absolute value of MR into the Verwey transition and then decrease after. The low-temperature MR's sign changes are due to the expected weak antilocalization since Pt is a high spin-orbit coupling metal. This is further observed in heterostructures of BPIO/Gr/Al, shown in figure S5

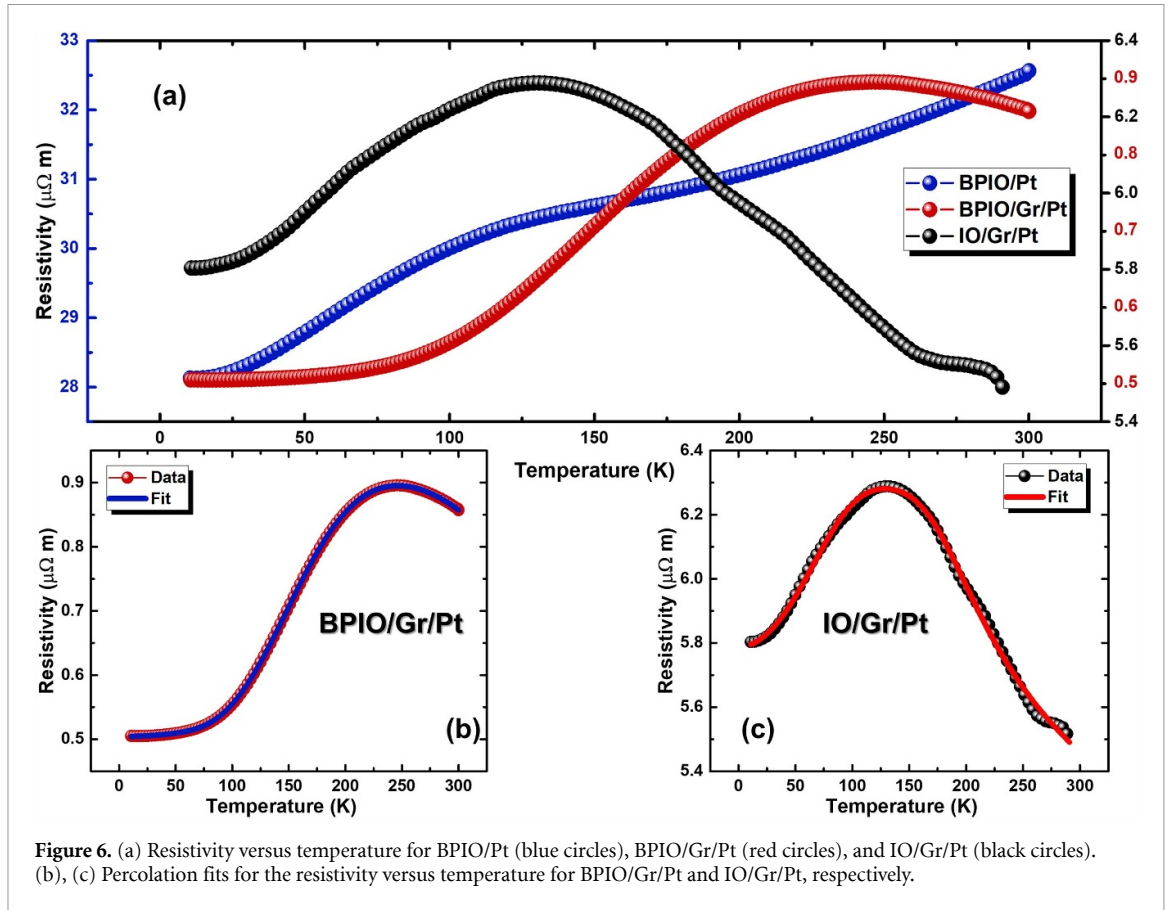


Figure 6. (a) Resistivity versus temperature for BPIO/Pt (blue circles), BPIO/Gr/Pt (red circles), and IO/Gr/Pt (black circles). (b), (c) Percolation fits for the resistivity versus temperature for BPIO/Gr/Pt and IO/Gr/Pt, respectively.

where negligible weak antilocalization is expected due to the low spin orbit coupling of Al. It can also be seen that magnetoresistive switching occurs in the BPIO/Gr/Al system as well, although complicated by the existence of oxidized aluminum at the top layer which may act like a tunnel barrier reducing the working current across the heterostructure. Nonetheless, switching is observed underscoring the importance of the iron oxide/graphene interface in these heterostructures. It is also important to note that in traditional IO or BPIO/Pt systems the dominant MR mechanism is spin-Hall MR [8, 36, 37]. The existence of switching in films capped with Al suggests that this is small as compared to the other magnetoresistive effects highlighted below since Al has a much smaller spin-Hall angle compared to Pt due to its small spin-orbit coupling (low Z).

To further explore the changes in the transport properties due to the inclusion of graphene, resistivity versus temperature ($\rho(T)$) measurements were performed. Figure 6(a) shows the $\rho(T)$ for BPIO/Pt (blue), BPIO/Gr/Pt (red), and IO/Gr/Pt (black). The BPIO/Pt film exhibits a trend similar to that reported previously [18]. The resistivity versus temperature for the samples with Gr both show peaks, appearing as a quasi-metal-insulator transition, where quasi refers to the nature of this transition being interfacial, not necessarily corresponding to the bulk heterostructure. This behavior is reminiscent of the CMR behavior that has been observed historically in doped manganites [48]. These peaks appear to occur near the temperatures in which the MR changes signs in each sample. To further explore the potential scattering mechanisms which can give rise to the temperature dependence of the resistivity, a percolative transport model has been proposed similar to what has been observed in doped manganites as a potential mechanism which can give rise to this behavior [49, 50]. Here, the percolation model is applied as regions of distinct conduction between the Pt overlayer and the proximitized Gr, which is hypothesized to hybridize with oxygen at the interface in insulating regions. This phenomenon has been studied experimentally and theoretically previously, showing that at insulating, oxygen rich interfaces such as NiFe_2O_4 , Gr hybridizes with the oxygen, greatly modifying the interfacial magnetic properties of the underlying magnetic substrate [24, 46, 51–53]. Importantly for the case of graphene it has been reported that these interfacial magnetic effects can be respectively large, leading to scattering mechanisms which can be on the order of other effects and accessible at finite temperatures. Here, IO and BPIO are only purely insulating below T_v . In the BPIO samples, however, the hematite phase is insulating across all temperatures of interest. Due to the separation between Pt and IO or BPIO induced by the inclusion of

Table 1. Extracted fit parameters for the BPIO/Gr/Pt and IO/Gr/Pt films.

	$\frac{U_0}{k_B}$ (K)	$\frac{E_g}{k_B}$ (K)	T_p (K)
BPIO/Gr/Pt	896 ± 2.56 K	443 ± 4.50 K	254 ± 0.86 K
IO/Gr/Pt	1521 ± 39.37 K	318 ± 7.40 K	182 ± 2.51 K

Gr, it appears that most of the induced interfacial magnetic phenomena occurs between Gr and IO or BPIO and possibly a few atomic layers of Pt [8, 54, 55]. This creates two distinct current channels. Pt at the surface acts as a metallic, PM metal, whereas current flowing closer to its interface with Gr acts as a magnetically proximitized semiconducting region, above T_v . Following closely with previous works [49, 50, 56], these distinct regions lead to competing localization and delocalization of charge carriers, with volume fractions f and $(1-f)$. Therefore, the total resistivity of Pt can be written as

$$\rho_{\text{Tot}} = \rho_{\text{Met}}f + \rho_{\text{Sem}}(1-f), \quad (1)$$

with ρ_{Met} and ρ_{Sem} are the metallic and semiconducting resistivity parts, respectively.

The metallic resistivity (ρ_{Met}) can be expressed as a combination of different scattering terms as:

$$\rho_{\text{Met}} = \rho_0 + \rho_2 T^2 + \rho_5 T^5, \quad (2)$$

where ρ_0 is the temperature-independent residual resistivity, ρ_2 corresponds to electron–electron scattering, and ρ_5 corresponds to electron-phonon scattering. For the interfacial current channel, it has been reported previously that Gr-based interfacial bonding occurs from the out of plane p_z orbitals of Gr [24, 46, 57]. This is particularly the case for lightly disordered Gr, where there exists non-zero out-of-plane phonon excitations, which is traditionally induced when sputtering onto Gr [24]. In the systems discussed here, this disorder is likely not in the form of metal overlayer implantation as films capped with both Pt and Al exhibit switching, but potentially comes in the form of disrupted carbon bonds. This interfacial hybridization can change the effective mass of local charge carriers compared to those in other regions, leading to magnetic polaron formation [58, 59]. Similar interfacial hybridization has also been studied in the context of using Gr as a charge trap [60]. Therefore, the total resistivity of the semiconducting phase can be expressed as:

$$\rho_{\text{Sem}} = \rho_{\text{SPH}} T e^{\frac{E_g}{k_B T}} \quad (3)$$

where ρ_{SPH} is the coefficient of resistivity due to single polaron hopping and E_g is the polaron activation energy. The relative volume fractions of each phase can then be modeled as a Boltzmann volume fraction as:

$$f = \frac{1}{1 + e^{\frac{\Delta U}{k_B T}}} \quad (4)$$

ΔU is the energy difference between the respective phases and can be expanded as a Taylor series about T_p :

$$\Delta U \approx -U_0 \left(1 - \frac{T}{T_p} \right) \quad (5)$$

The aforementioned definitions can then be placed into the expression for the total resistivity to fit the temperature dependence of the resistivity. Figures 6(b) and (c) show the fits of this model for BPIO/Gr/Pt, and IO/Gr/Pt, respectively. It can be seen that the proposed model is in excellent agreement with the measured data ($R^2 \sim 1$). Furthermore, important fit parameters can be extracted and are listed in table 1.

The extracted fit parameters indicate larger energy difference between the two phases corresponding to lower switching temperatures. This further agrees with the hypothesis that adjusting the relative volume fractions of hematite allows for the control of the switching temperature in these films, with the single-phase IO/Gr/Pt sample acting as a limiting case in which the temperature is lowest. Finally, lower polaron formation energies correspond to a higher energy difference between the two phases, which agrees with the argument regarding the phase segregation in these films.

3. Conclusion

Films of variable phase iron oxide (magnetite or hematite) were deposited to study their interface with graphene. The relative phases were confirmed independently by XRD and Raman spectroscopy measurements. The inclusion of Gr appears to dampen the characteristic Verwey transition of magnetite. To probe the interface between Gr and IO or BPIO, MR and resistivity measurements were performed. We observe that by the inclusion of Gr, switching of the MR from negative at high temperatures to positive at low temperatures occurred. Resistivity versus temperature measurements further show a peak indicative of a quasi-metal-insulator transition at the same temperatures. A percolative transport model is proposed to explain the observed behavior. This model agrees excellently with the experimental results and implies that the magnetoresistive switching and peaks occur due to Gr-induced competition between localization and delocalization of charge carriers arising from Gr hybridization at the interface in the insulating phase. This behavior can be further tuned by controlling the energy difference between the respective phases, which depends strongly on the volume fraction of hematite. Future experiments including corresponding transport measurements like temperature dependent anomalous Hall measurements as well as surface sensitive magnetic measurements like x-ray magnetic circular dichroism would be helpful in fully elucidating the interfacial phenomena in these systems. These novel interfacial phenomena can be utilized to create magnetoresistive switching devices on CMOS-compatible substrates through the inclusion of monolayer Gr for applications in modern devices and neuromorphic computing.

4. Experimental methods

Iron oxide(s) growth

Iron oxide films were grown using a KrF laser and stoichiometric Fe_3O_4 target. Fe_3O_4 sample set 1 was grown using a laser fluence of 2.5 J cm^{-2} , $350 \text{ }^\circ\text{C}$ substrate temperature, 5 Hz laser repetition rate, target substrate distance of 5 cm , using the Fe_3O_4 target, and a background pressure of $2 \times 10^{-5} \text{ Torr O}_2$. Fe_3O_4 sample set 2 and $\text{Fe}_3\text{O}_4/\text{MgO}$ were grown using the same parameters, with a change in fluence to 2.25 J cm^{-2} . XRD data were collected using a Rigaku Smartlab diffractometer to measure crystal structure.

Graphene transfer

The commercially available mono-layer CVD graphene purchased from graphene was transferred onto BPIO films using a wet transfer method. The CVD graphene on a polymer layer covered with a protective sacrificial PMMA layer was dipped into DI water at an angle of 45° . The floating graphene with the PMMA sacrificial layer was carefully scooped onto the BPIO film. The BPIO films with transferred graphene were then kept on an oblique stand for 1 h for air drying to avoid any wrinkles or trapped air bubbles on the graphene. To obtain a strong adhesion between the graphene and BPIO films, the graphene/BPIO samples were kept in a vacuum desiccator for 24 h , followed by subsequent annealing at $150 \text{ }^\circ\text{C}$ for 2 h . Finally, the protective sacrificial PMMA layer was removed by dissolving the PMMA layer in an acetone bath at $50 \text{ }^\circ\text{C}$ for 1 h , subsequently rinsed with isopropanol, and dried. The quality of the transferred graphene on BPIO was confirmed by checking them with an optical microscope (Olympus AX70) and an AFM (Bruker-Dimension Icon ICON4-SYS). The final graphene/BPIO heterostructures were used for further characterization and electrical and magnetic measurements (with/without depositing a 5 nm thin Pt layer on top of them).

Platinum deposition

Pt deposition was carried out in an Intlvac Nanochrome Pico magnetron sputtering system at room temperature with base pressure below $2.7 \times 10^{-7} \text{ mbar}$ before initiating D.C sputtering, ultra-high-purity argon gas was introduced into the chamber at a flow rate of 30 sccm . In order to reduce the effect of Pt sputtering on the Gr layer a low power/deposition rate sputtering process was utilized. The Pt target was ignited at 20 W , followed by a 6 min conditioning and presputtering process. Subsequently, the 5 nm Pt film was deposited at a working pressure of $9.7 \times 10^{-3} \text{ mbar}$, with a deposition rate of 0.12 \AA s^{-1} . The sample was rotated during deposition to achieve homogeneous growth.

Raman spectroscopy

Raman spectroscopy experiments were conducted using a confocal microscope-based Raman spectrometer (LabRAM HR Evolution, Horiba Scientific) with 600 gr mm⁻¹ diffraction grating, a 633 nm excitation laser beam, a 100× objective, and a synapse back-illuminated CCD.

XRD

XRD data were collected using a Rigaku Smartlab diffractometer to measure crystal structure, sweeping out-of-plane with respect to the sample surface.

Magnetometry

Magnetization versus magnetic field and temperature measurements were performed utilizing the vibrating sample magnetometer option of a physical properties measurement system (PPMS), Quantum Design, USA. For the magnetization versus temperature measurements, a ZFC/ FC protocol was followed in which the system was cooled under the presence of zero magnetic field, then a magnetic field was applied, and the magnetization was measured during warming. The FC protocol then measures the magnetization under the same field while cooling after the ZFC measurement is completed. The magnetization versus magnetic field measurements were performed in an in-plane orientation with respect to the applied magnetic field, and the data was corrected with respect to the substrate and rod background by removing a linearly proportional negative diamagnetic background.

Magnetotransport

Resistivity versus temperature and MR measurements were performed on a universal puck, utilizing the resistivity option within the same PPMS. All field dependent measurements were performed under an out-of-plane applied magnetic field. Electrical connections were made in a standard four-point configuration on the surface of the Pt layer, with contacts attached with high purity silver paint.

Acknowledgment

Work at USF was supported by the US Department of Energy, Office of Basic Energy Sciences, Division of Materials Science and Engineering Grant No. DE-FG02-07ER46438 (Growth of iron oxide films; structural, magnetic, and magneto-transport studies). N.S would like to acknowledge funding from the Department of Defense SMART program. T.S gratefully acknowledges funding from the Swedish Research Council (Grant No. 2021-03675). M.V.K and G.D gratefully acknowledge funding from European Research Council (ERC) Project SPINNER (Grant No. 101002772), Stiftelsen Olle Engkvist Byggmästare (200–0602), Formas (2023-01607), and Knut and Alice Wallenberg Foundation (Grants Nos. 2022.0079 and 2023.0336).

Data availability statement

Our data will be available upon reasonable request, but we will not be uploading our raw data to any public repository due to concerns about AI tools being used in scientific publishing.

Supplementary data 1 available at <https://doi.org/10.1088/1361-648X/ae58e1/data1>.

Conflict of interest

The authors declare that they have no known competing financial interests or personal relationships that could have appeared to influence the work reported in this paper.

ORCID iDs

N Schulz  0000-0002-8639-3073

A Chanda  0000-0001-9681-0312

A Ojo  0009-0006-1083-6241

D A Arena  0000-0001-7463-6472

H R Gutierrez  0000-0001-8997-5274

M V Kamalakar  0000-0003-2385-9267

M H Phan  0000-0002-6270-8990

H Srikanth  0000-0002-2541-7000

References

- [1] Sakurai S, Namai A, Hashimoto K and Ohkoshi S 2009 First observation of phase transformation of all four Fe₂O₃ phases ($\gamma \rightarrow \epsilon \rightarrow \beta \rightarrow \alpha$ -Phase) *J. Am. Chem. Soc.* **131** 18299–303
- [2] Ramos R et al 2013 Observation of the spin seebeck effect in epitaxial Fe₃O₄ thin films *Appl. Phys. Lett.* **102** 072413
- [3] Cava C E, Possagno R, Schnitzler M C, Roman P C, Oliveira M M, Lepiensky C M, Zarbin A J G and Roman L S 2007 Iron- and iron oxide-filled multi-walled carbon nanotubes: electrical properties and memory devices *Chem. Phys. Lett.* **444** 304–8
- [4] Wang Z and Liu C-J 2015 Preparation and application of iron oxide/graphene based composites for electrochemical energy storage and energy conversion devices: current status and perspective *Nano Energy* **11** 277–93
- [5] Xu C, Akakuru O U, Zheng J and Wu A 2019 Applications of iron oxide-based magnetic nanoparticles in the diagnosis and treatment of bacterial infections *Front. Bioeng. Biotechnol.* **7** 141
- [6] Yang X, Chen C, Li J, Zhao G, Ren X and Wang X 2012 Graphene oxide-iron oxide and reduced graphene oxide-iron oxide hybrid materials for the removal of organic and inorganic pollutants *RSC Adv.* **2** 8821–6
- [7] Xu P et al 2012 Use of iron oxide nanomaterials in wastewater treatment: a review *Sci. Total Environ.* **424** 1–10
- [8] Chanda A, Hung C-M, Tuan Duong A, Cho S, Srikanth H and Phan M-H 2023 Magnetism and spin-dependent transport phenomena across Verwey and Morin transitions in iron oxide/Pt bilayers *J. Magn. Magn. Mater.* **568** 170370
- [9] Zierold R, Lam C L, Dendooven J and Walz F 2002 The Verwey transition—a topical review *J. Phys.: Condens. Matter* **14** R285–340
- [10] Pastor J M, Pérez-Landazábal J I, Gómez-Polo C, Recarte V, Larumbe S, Santamarta R, Fernandes Silva M, Gómez Pineda E A, Winkler Hechenleitner A A and Lima M K 2012 Entropy change linked to the magnetic field induced Morin transition in hematite nanoparticles *Appl. Phys. Lett.* **100** 063102
- [11] Attanayake S B, Chanda A, Das R, Phan M H and Srikanth H 2023 Effects of annealing temperature on the magnetic properties of highly crystalline biphasic iron oxide nanorods *AIP Adv.* **13** 025333
- [12] Shimomura N, Pati S P, Sato Y, Nozaki T, Shibata T, Mibu K and Sahashi M 2015 Morin transition temperature in (0001)-oriented α -Fe₂O₃ thin film and effect of Ir doping *J. Appl. Phys.* **117** 17C736
- [13] Mibu K, Mikami K, Tanaka M, Masuda R, Yoda Y and Seto M 2017 Thickness dependence of Morin transition temperature in iridium-doped hematite layers studied through nuclear resonant scattering *Hyperfine Interact.* **238** 92
- [14] Condon N G, Leibsle F M, Lennie A R, Murray P W, Vaughan D J and Thornton G 1995 Biphasic ordering of iron oxide surfaces *Phys. Rev. Lett.* **75** 1961–4
- [15] Serrano A, Rubio-Zuazo J, López-Sánchez J, Arnay I, Salas-Colera E and Castro G R 2018 Stabilization of epitaxial α -Fe₂O₃ thin films grown by pulsed laser deposition on oxide substrates *J. Phys. Chem. C* **122** 16042–7
- [16] Li X W, Gupta A, Xiao G and Gong G Q 1998 Transport and magnetic properties of epitaxial and polycrystalline magnetite thin films *J. Appl. Phys.* **83** 7049–51
- [17] Attanayake S B, Chanda A, Das R, Phan M H and Srikanth H 2022 Emergent magnetic properties of biphasic iron oxide nanorods *AIP Adv.* **12** 035136
- [18] Chanda A et al 2022 Spin seebeck effect in iron oxide thin films: effects of phase transition, phase coexistence, and surface magnetism *ACS Appl. Mater. Interfaces* **14** 13468–79
- [19] Qu Q, Yang S and Feng X 2011 2D sandwich-like sheets of iron oxide grown on graphene as high energy anode material for supercapacitors *Adv. Mater.* **23** 5574–80
- [20] Wallace P R 1947 The band theory of graphite *Phys. Rev.* **71** 622–34
- [21] Pesin D and MacDonald A H 2012 Spintronics and pseudospintronics in graphene and topological insulators *Nat. Mater.* **11** 409–16
- [22] Novoselov K S, Geim A K, Morozov S V, Jiang D, Katsnelson M I, Grigorieva I V, Dubonos S V and Firsov A A 2005 Two-dimensional gas of massless Dirac fermions in graphene *Nature* **438** 197–200
- [23] Huertas-Hernando D, Guinea F and Brataas A 2006 Spin-orbit coupling in curved graphene, fullerenes, nanotubes, and nanotube caps *Phys. Rev. B* **74** 155426
- [24] Schulz N, Chanda A, Datt G, Kamalakar M V, Sarkar T, Phan M H and Srikanth H 2022 Proximity enhanced magnetism at NiFe₂O₄/graphene interface *AIP Adv.* **12** 035132
- [25] Karpiak B et al 2019 Magnetic proximity in a van der Waals heterostructure of magnetic insulator and graphene *2D Mater.* **7** 015026
- [26] Panda J, Ramu M, Karis O, Sarkar T and Kamalakar M V 2020 Ultimate spin currents in commercial chemical vapor deposited graphene *ACS Nano* **14** 12771–80
- [27] Younis M, Abdullah M, Dai S, Iqbal M A, Tang W, Sohail M T, Atiq S, Chang H and Zeng Y 2025 Magnetoresistance in 2D magnetic materials: from fundamentals to applications *Adv. Funct. Mater.* **35** 2417282
- [28] Smith L W et al 2022 Giant magnetoresistance in a chemical vapor deposition graphene constriction *ACS Nano* **16** 2833–42
- [29] Singla R, Shukla A S and Kottantharayil A 2021 Introducing ferromagnetism and anisotropic magnetoresistance in monolayer CVD graphene by nitrogen doping *Nanotechnology* **32** 205704
- [30] Liu Y, Yang R, Yang H, Wang D, Zhan Q, Zhang G, Xie Y, Chen B and Li R-W 2014 Anomalous anisotropic magnetoresistance effects in graphene *AIP Adv.* **4** 097101
- [31] Abanin D A et al 2011 Giant nonlocality near the Dirac point in graphene *Science* **332** 328–30
- [32] Zhang G, Wu H, Yang L, Jin W, Zhang W and Chang H 2024 Graphene-based spintronics *Appl. Phys. Rev.* **11** 021308
- [33] Godel F, Venkata Kamalakar M, Doudin B, Henry Y, Halley D and Dayen J-F 2014 Voltage-controlled inversion of tunnel magnetoresistance in epitaxial nickel/graphene/MgO/cobalt junctions *Appl. Phys. Lett.* **105** 152407
- [34] Belotckercovtceva D, Maciel R P, Berggren E, Maddu R, Sarkar T, Kvashnin Y O, Thonig D, Lindblad A, Eriksson O and Kamalakar M V 2022 Insights and implications of intricate surface charge transfer and Sp³-defects in graphene/metal oxide interfaces *ACS Appl. Mater. Interfaces* **14** 36209–16
- [35] Ziese M and Blythe H J 2000 Magnetoresistance of Magnetite *J. Phys.* **12** 13–28
- [36] Pham T K H et al 2018 Interface morphology effect on the spin mixing conductance of Pt/Fe₃O₄ bilayers *Sci. Rep.* **8** 13907

- [37] Scheufele M 2021 Tuning the amplitude of the spin Hall magnetoresistance *Masters Thesis* Walther-Meißner-InstitutWalther-Meißner-Institut
- [38] Webster P J 1971 Magnetic and chemical order in Heusler alloys containing cobalt and manganese *J. Phys. Chem. Solids* **32** 1221–31
- [39] Zener C 1951 Interaction between the d-shells in the transition metals. II. Ferromagnetic compounds of manganese with perovskite structure *Phys. Rev.* **82** 403–5
- [40] Amara G M, Dhahri A, Dhahri J and Hlil E K 2017 Correlation between magnetic and electric properties based on the critical behavior of resistivity and percolation model of $\text{La}_{0.8}\text{Ba}_{0.1}\text{Ca}_{0.1}\text{MnO}_3$ polycrystalline *RSC Adv.* **7** 10928–38
- [41] Lübke M, Gigler A M, Stark R W and Moritz W 2010 Identification of iron oxide phases in thin films grown on $\text{Al}_2\text{O}_3(0001)$ by Raman spectroscopy and x-ray diffraction *Surf. Sci.* **604** 679–85
- [42] Qiu X P, Shin Y J, Niu J, Kulothungasagaran N, Kalon G, Qiu C, Yu T and Yang H 2012 Disorder-free sputtering method on graphene *AIP Adv.* **2** 032121
- [43] Attanayake S B, Chanda A, Hulse T, Das R, Phan M-H and Srikanth H 2023 Competing magnetic interactions and field-induced metamagnetic transition in highly crystalline phase-tunable iron oxide nanorods *Nanomaterials* **13** 1340
- [44] Liu X, Lu H, He M, Wang L, Shi H, Jin K, Wang C and Yang G 2014 Room-temperature layer-by-layer epitaxial growth and characteristics of Fe_3O_4 ultrathin films *J. Phys. D: Appl. Phys.* **47** 105004
- [45] Coey J M D, Berkowitz A E, Balcells L, Putris F F and Parker F T 1998 Magnetoresistance of magnetite *Appl. Phys. Lett.* **72** 734–6
- [46] Schulz N et al 2023 Surface termination-enhanced magnetism at nickel Ferrite/2D nanomaterial interfaces: implications for spintronics *ACS Appl. Nano Mater.* **6** 10402–12
- [47] Jain A et al 2013 Commentary: the materials project: a materials genome approach to accelerating materials innovation *APL Mater.* **1** 011002
- [48] Tokura Y and Tomioka Y 1999 Colossal magnetoresistive manganites *J. Magn. Magn. Mater.* **200** 1–23
- [49] Das S and Dey T K 2005 Electrical conductivity and low field magnetoresistance in polycrystalline $\text{La}_{1-x}\text{K}_x\text{MnO}_3$ pellets prepared by pyrophoric method *Solid State Commun.* **134** 837–42
- [50] Hcini S, Khadhraoui S, Zemni S, Triki A, Rahmouni H, Boudard M and Oumezzine M 2013 Percolation model of the temperature dependence of resistivity in $\text{Pr}_{0.67}\text{A}_{0.33}\text{MnO}_3$ (A=Ba or Sr) manganites *J. Supercond. Nov. Magn.* **26** 2181–5
- [51] Abtew T, Shih B-C, Banerjee S and Zhang P 2013 Graphene–ferromagnet interfaces: hybridization, magnetization and charge transfer *Nanoscale* **5** 1902
- [52] Hallal A, Ibrahim F, Yang H, Roche S and Chshiev M 2017 Tailoring magnetic insulator proximity effects in graphene: first-principles calculations *2D Mater.* **4** 025074
- [53] Yang H X, Hallal A, Terrade D, Waintal X, Roche S and Chshiev M 2013 Proximity effects induced in graphene by magnetic insulators: first-principles calculations on spin filtering and exchange-splitting gaps *Phys. Rev. Lett.* **110** 046603
- [54] Thi-Xuan Dang D, Barik R K, Phan M-H and Woods L M 2022 Enhanced magnetism in heterostructures with transition-metal dichalcogenide monolayers *J. Phys. Chem. Lett.* **13** 8879–87
- [55] Park J, Oh I, Lee A-Y, Jang H, Yoo J-W, Jo Y and Park S-Y 2020 The effect of graphene interlayer at Pt/YIG interface on spin pumping *J. Alloys Compd.* **829** 154534
- [56] Yuan S L et al 2000 Origins of both insulator–metal transition and colossal magnetoresistance in doped manganese perovskites *Appl. Phys. Lett.* **77** 4398–400
- [57] Weser M, Rehder Y, Horn K, Sicot M, Fonin M, Preobrajenski A B, Voloshina E N, Goering E and Dedkov Y S 2010 Induced magnetism of carbon atoms at the graphene/Ni(111) interface *Appl. Phys. Lett.* **96** 012504
- [58] Pandey S, Hettler S, Arenal R, Bouillet C, Moghe A R, Berciaud S, Robert J, Dayen J-F and Halley D 2023 Room-temperature anomalous Hall effect in graphene in interfacial magnetic proximity to EuO grown by topotactic reduction *Phys. Rev. B* **108** 144423
- [59] Anil Kumar P et al 2020 Magnetic polarons and spin-glass behavior in insulating $\text{La}_{1-x}\text{Sr}_x\text{CoO}_3$ ($x=0.125$ and 0.15) *Phys. Rev. Res.* **2** 043344
- [60] Maciel R P, Eriksson O, Kvashnin Y O, Thonig D, Belotckercovtceva D, Kamalakar M V and Ong C S 2023 Resistive switching in graphene: a theoretical case study on the alumina-graphene interface *Phys. Rev. Res.* **5** 043147